**Shannen B. Kizilski**
Department of Mechanical Engineering,
University of Minnesota,
312 Church Street SE Hasselmo Hall, 7-105,
Minneapolis, MN 55455
e-mail: kizil015@umn.edu

**Omid Amili**
Mem. ASME
Department of Aerospace
Engineering and Mechanics,
University of Minnesota,
110 Union Street SE Akerman Hall,
Minneapolis, MN 55455
e-mail: oamili@umn.edu

**Filippo Coletti**
Department of Aerospace
Engineering and Mechanics,
University of Minnesota,
110 Union Street SE Akerman Hall,
Minneapolis, MN 55455
e-mail: fcoletti@umn.edu

**Rumi Faizer**
Department of Surgery,
University of Minnesota,
909 Fulton Street SE,
Minneapolis, MN 55455
e-mail: rfaizer@umn.edu

**Victor H. Barocas**
Fellow ASME
Department of Biomedical Engineering,
University of Minnesota,
312 Church Street SE Hasselmo Hall, 7-105,
Minneapolis, MN 55455
e-mail: baroc001@umn.edu

# Conceptual Framework Development for a Double-Walled Aortic Stent-Graft to Manage Blood Pressure

*A double-walled stent-graft (DWSG) design with a compressible gas layer was conceived with the goal of treating hypertension in patients receiving an aortic stent-graft. Early prototypes were developed to evaluate the design concept through static measurements from a finite element (FE) model and quasi-static inflation experiments, and through dynamic measurements from an in vitro flow loop and the three-element Windkessel model. The amount of gas in the gas layer and the properties of the flexible inner wall were the primary variables evaluated in this study. Properties of the inner wall had minimal effect on DWSG behavior, but increased gas charge led to increased fluid capacitance and larger reduction in peak and pulse pressures. In the flow loop, placement of the DWSG decreased pulse pressure by over 20% compared to a rigid stent-graft. Capacitance measurements were consistent across all methods, with the maximum capacitance estimated at 0.07 mL/mmHg for the largest gas charge in the 15 cm long prototype. Windkessel model predictions for in vivo performance of a DWSG placed in the aorta of a hypertensive patient showed pulse pressure reduction of 14% compared to a rigid stent-graft case, but pressures never returned to unstented values. These results indicate that the DWSG design has potential to be developed into a new treatment for hypertensive patients requiring an aortic intervention.* [DOI: 10.1115/1.4047873]

## 1 Introduction

Chronic high blood pressure, or hypertension, affects about one third of the adult U.S. population [1]. Multiple studies have shown a strong link between hypertension and more serious cardiovascular diseases including stroke and ischemic heart disease [1–4]. Although a variety of factors may contribute to the development of hypertension, the present work focuses on the role of aortic stiffening.

The aorta, the largest artery in the human body, plays an essential role in conducting oxygenated blood from the heart to the visceral organs and major branching vessels. When an injury develops in the aorta, either due to trauma or a chronic condition, primary intervention focuses on preventing vessel rupture and maintaining adequate blood flow. The most common types of aortic implants are grafts and stent-grafts [5,6]. Aortic grafts are flexible fabric tubes that are sewn end-to-end with the native aorta to replace a damaged portion that has been excised. Stent-grafts, which are fabric tubes reinforced with metal wires, are delivered via an endovascular catheter and deployed to push against the internal wall of the damaged aortic segment. Rather than completely replacing a length of the aorta, a stent-graft resides within the native vessel and provides structural support to prevent occlusion or rupture. Stent-graft procedures have been gaining popularity over open surgery in recent years due to reduced morbidity and mortality [7].

Aside from its role as a conduit, the aorta plays a crucial role as a reservoir in the arterial system. The elasticity of a healthy aorta allows it to expand and contract with each heartbeat, storing and releasing blood during cardiac systole and diastole, respectively. By temporarily storing blood, the aorta promotes a steadier flow to the peripheral vessels, thereby reducing the swing between systolic and diastolic pressures, also known as the pulse pressure. Increased aortic stiffness, which occurs naturally with age, has been identified as an independent risk factor for cardiovascular events [8]. It has also been shown that increased arterial stiffness is associated with increased blood pressure, due to increased wave speed and pulsatility [9].

The capacitive function of the aorta has long been recognized and quantified by both the scientific and medical communities, yet it has been largely neglected in existing graft and stent-graft designs. Dacron (polyethylene terephthalate) and other materials commonly used for graft fabric are more than 20 times stiffer than the healthy aortic wall [10]. The radial stiffness of a stent-graft ensures that it protects the damaged aortic wall from pressure-induced injury or rupture, but it also inhibits storage and release of blood in that segment. With more studies emerging about the long-term health effects of stent-grafts, it is becoming apparent that matching aortic conductance alone is an insufficient standard [11].

Manuscript received October 1, 2019; final manuscript received June 3, 2020; published online July 31, 2020. Assoc. Editor: Kunal Mitra.

 Copyright © 2020 by ASME 

Incorporating both protection of the aortic wall and significant fluid capacitance into a single stent-graft design is not a trivial task—protection requires that the aorta is not subjected to large oscillatory strains, but capacitance requires that the lumen volume changes with blood pressure. Another difficulty arises when we consider the fact that many patients receiving stent-grafts already have a significantly stiffened aorta, which cannot provide the capacitance seen in a healthy individual [12,13]. Approximately 40% of patients receiving stent-grafts to treat dissection in the descending thoracic aorta are over 65 years of age [14], at which point the aorta is more than twice as stiff as that of a young, healthy individual [15]. The optimal stent-graft would shield the aorta from stresses due to blood pressure *and* still would permit changes in lumen volume in response to pressure changes, even if the aortic wall itself cannot adequately stretch and recoil.

Efforts to develop a more compliant stent-graft to better mimic the capacitive function of the healthy aorta are limited by the extrinsic constraints of the existing diseased aorta. First, if the device is in direct contact with the aortic wall along its entire length, as is usually the case in the treatment of aortic dissection, the overall compliance and capacitive characteristics of that aortic segment are *at best* defined by the diseased, native aortic wall, regardless of the graft material used. Simply put, the stent-graft cannot make the native aortic wall (with which it is in contact) *more* compliant, only less. In practice, all existing stent-grafts have been demonstrated to add significantly to aortic rigidity [16]. Furthermore, if the stent-graft is not in direct contact with the aortic wall except for fixation at its two ends, as may be the case with an aortic aneurysm, or where a stent-graft is theoretically designed to be narrower in its central section to prevent direct wall apposition with the native aorta, the intervening space will be filled with blood. If the stent-graft works as intended, this blood will not flow and will clot, forming a chronic thrombus, which is virtually incompressible [17], again removing any capacitive potential. The clinical scenario in which thrombus formation does not occur—so the space between the stent-graft and the aortic wall contains flowing blood—is considered a clinical failure termed endoleak, as it exposes the damaged aortic wall to ongoing pressurization and risk of rupture [18].

In this paper, we present a novel, double-walled stent-graft (DWSG) design which aims to address the issue of aortic capacitance loss [19]. By introducing a permanent, compressible gas interface between the aortic wall and an inner compliant lumen, we intend to introduce a capacitive chamber that better resembles healthy aortic function. An early prototype of the design was evaluated through pressure measurements in static and pulsatile flow experiments. The results of these experiments were used to develop more accurate computational models of the design and to facilitate more thorough parameter optimization.

## 2 Methods

Figure 1 outlines the inputs and outputs to the models and experiments that were used to characterize the DWSG and its predicted effect on cardiovascular health. Details of the DWSG design, experimental methods, and computational models are described in the following sections.

**2.1 Device Design.** The long-term objective of this investigation is to develop a new stent-graft design capable of maintaining or lowering blood pressure in patients requiring aortic repair. An implant designed to help control blood pressure could reduce patient dependence on antihypertensive medications and lower risk for subsequent cardiovascular events. The goal of the proposed design is to counteract high blood pressure by partially restoring fluid capacitance lost due to vascular stiffening and stent-graft rigidity. One key requirement for the design is that it be an endovascular device, which would reside within the lumen of the native aorta. Based on this constraint, it is necessary that the capacitive function operate within a completely rigid aortic wall. To this end, we needed to investigate whether the aorta could tolerate some reduction in lumenal area, if the reduced area facilitated increased capacitance. Compared to the rest of the arterial system, the aorta has negligible flow resistance; if the lumen were reduced in diameter by a small percentage, we hypothesize that this area could be used to incorporate capacitance without introducing significant flow resistance.

Fluid capacitance $C$ is defined as the derivative of fluid volume stored in the lumen, $V_{\text{lumen}}$, with respect to lumen pressure, $P_{\text{lumen}}$ (Eq. (1)) [20].

$$C = \frac{dV_{\text{lumen}}}{dP_{\text{lumen}}} \tag{1}$$

If we assume the stent-graft will occupy a fixed length of the aorta, then the only way to vary the stored volume of fluid within that fixed length is to vary the lumen radius. Assuming a fixed outer wall, corresponding to the nearly rigid native aorta, or the rigid stent-graft that protects the injured aorta from cyclic loading, variable lumen radius can only be achieved by a compressible layer *within* the stent-graft.

We propose a DWSG design, which incorporates a compressible layer of carbon dioxide ($CO_2$) gas between a stiff outer wall and a flexible, elastic inner wall (Fig. 2(*a*)). The outer wall, like existing stent-grafts, holds the device in place and protects the diseased aortic wall from pressure-induced injury. The inner wall passively transmits the lumenal pressure to the contained gas, which consequently compresses during systole and expands during diastole. According to the Ideal Gas Law, a gas subjected to normal blood pressure levels (120/80 mmHg) should experience a roughly 5% volume change between systole and diastole (40 mmHg change in pressure versus approximately 860 mmHg absolute pressure); because the DWSG is targeted at patients with high blood pressure, a 5% volume change is a conservative estimate.

The rationale for including a layer of $CO_2$ gas within the device is that there must be some compressible material separating the

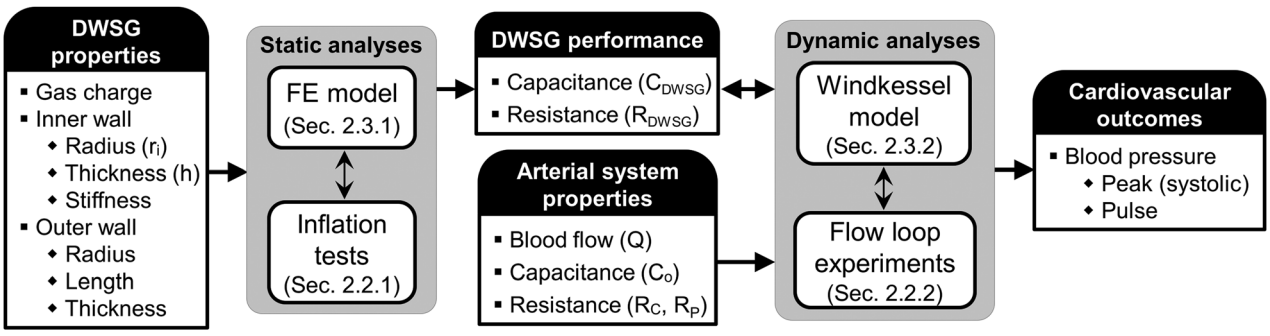



**Fig. 1 Flowchart depicting the procedure followed to characterize the DWSG and predict its performance. The sections of this paper that describe each method are denoted, when applicable.**

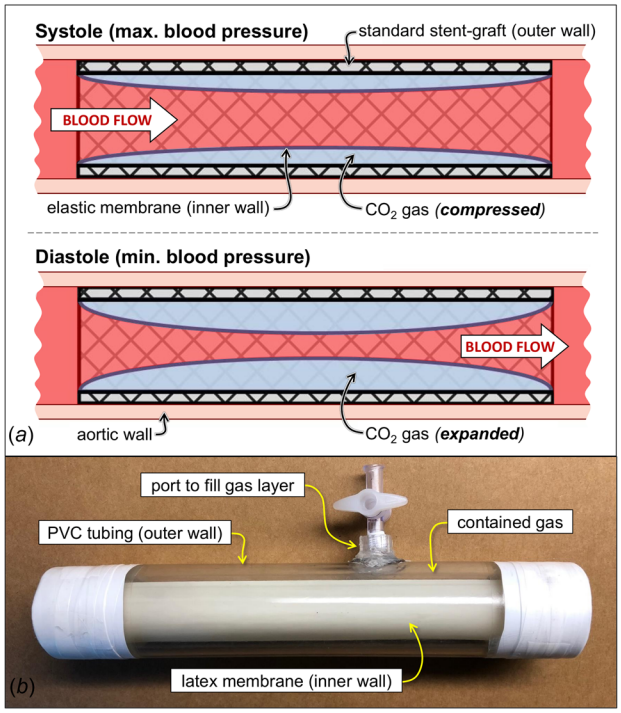



**Fig. 2 (*a*) Diagram of the DWSG design, with a stiff outer wall pushing radially outward against the aortic wall and a flexible inner wall containing a gas layer. (*b*) Photo of the DWSG prototype (15 cm length) used for the static and dynamic experiments. Latex tubes with different diameters and prestretches were used to achieve a range of inner wall properties.**

two walls in order for the device to have capacitive behavior. If a liquid were used instead, then the inner elastic wall would not be able to expand due to the incompressible nature of liquid. If all material were evacuated from that space, a vacuum would form, causing the elastic wall to get pressed directly against the stiff, outer wall. Filling the space with a compressible gas is the most practical way to achieve local capacitance. Specifically, $CO_2$ was chosen due to its ability to absorb safely into the bloodstream [21]. Any other biocompatible gas would be an adequate substitute.

The primary variables of interest in the DWSG design are the amount of gas contained, the overall length of the device, and properties of the inner wall, including stiffness, thickness, and unloaded diameter. The properties of the outer wall are not critical to device function because this wall only serves as an anchor for the device, holding it fixed against the stiff aortic wall. As explained earlier, any compliance in the outer wall of the DWSG is overridden by the stiffness of the aorta. In this study, the outer wall properties and the overall length of the device were kept constant, and the effects of the amount of gas and inner wall properties were evaluated.

Prototypes of the DWSG (Fig. 2(*b*)) were built using stiff 2.54 cm (1 in.) diameter PVC tubing for the outer wall and a thin latex tube (Penrose drain) with a diameter of 1.9 cm (3/4 in.), 2.22 cm (7/8 in.), or 2.54 cm (1 in), for the inner wall. In addition to being inexpensive and readily available, PVC is nearly rigid under the loading conditions considered; thus, it represents the worst-case scenario in which the surrounding vessel wall and/or stent-graft wall offer no compliance, and all flow capacitance must come from compression of the gas layer. Devices were assembled by threading the latex tube through the lumen of the PVC tube and stretching either end of the latex tube around the outside of the PVC, creating a sealed space between the two layers. Prototypes were built with the latex tube prestretched to 5% and 50% to artificially create inner walls with different stiffnesses. The ends of the latex tube were anchored using PTFE tape and a layer of Parafilm (Sigma-Aldrich, Merck KGaA, Darmstadt, Germany) to secure the tape. A port in the wall of the PVC tube was connected to an external luer lock valve, which was used to add or remove gas from the space between the two tubes. Although $CO_2$ would be the preferred gas in an in vivo device, tests were conducted using atmospheric air due to its similar mechanical behavior and ample availability.

**2.2 Experimental Methods.** Prototypes of the DWSG were tested in static inflation and in dynamic flow loop experiments. Through static inflation, the capacitance was measured and compared among different DWSG configurations, while changes in dynamic system pressure were observed for different prototypes in the flow loop experiments.

*2.2.1 Static Inflation.* The capacitance of each DWSG prototype was calculated as defined by Eq. (1). Prototypes were fabricated with a total length of approximately 18 cm, but all tests were conducted with a standard length of 15 cm by mounting each prototype within the same fixture that had 2.54 cm (1 in.) diameter barbed hose connections with inlets spaced 15 cm apart. The fixture had caps on either end to create a closed system once the prototype was inserted. Two ports in the fixture were used for connection of (1) a syringe for addition and removal of fluid and (2) a pressure transducer (P55, Validyne Engineering, Northridge, CA) to record lumen pressure at each volume. All tests were conducted at room temperature.

For a given test, the DWSG prototype was mounted in the fixture using hose clamps. A syringe was used to fill the prototype with a given gas charge, which was recorded as the gas volume at atmospheric pressure. The lumen of the closed system was evacuated of air and filled with water. The pressure sensor was used to ensure that the lumen pressure was ultimately returned to atmospheric level, which was set as a zero point. A syringe pump (KD Scientific, Holliston, MA) mounted with a 10 mL syringe was used to add water to the lumen in 0.5 mL stepwise increments while the pressure was simultaneously recorded. Following 10 mL injection, or if lumen pressure approached the 300 mmHg limit of the pressure sensor, the pump was reversed to remove 0.5 mL increments of water until pressure returned to zero. This procedure was followed twice for each prototype for a total of four pressure measurements at each lumen volume. Measurements from the pressure sensor were collected with a MATLAB script (Mathworks, Natick, MA) via a USB-connected DAQ (MicroDAQ, Contoocook, NH). A volume–pressure curve was constructed for each prototype, and capacitance was calculated as a function of lumen pressure by finding the slope between adjacent points.

To estimate the flow resistance of the different DWSG prototypes, photos were taken down the lumen of the DWSG at each gas charge. The cross-sectional area of the lumen for each case was measured by tracing it in IMAGEJ [22]. These estimates were used to calculate flow resistance with Poiseuille's law, assuming constant cross section along the length of the prototype. We knew that the assumption of constant cross section would not be true in practice, but it provided a convenient and conservative (high) estimate of resistance.

*2.2.2 Flow Loop.* The goal of the flow loop experiments was to simulate implantation of the DWSG into the aorta to predict the effect of different configurations on blood pressure. The flow loop system (Fig. 3) consisted of a pulsatile flow pump, a compliant arch, a fixture for DWSG prototypes, flexible tubing, a needle valve, and a storage reservoir. The only component of the system that changed between experiments was the prototype placed in the fixture.

The pump (EnvivoPC, Maximum Fidelity Surgical Simulations) enabled control of the stroke volume and pulse rate. The compliant arch was constructed by painting layers of liquid latex

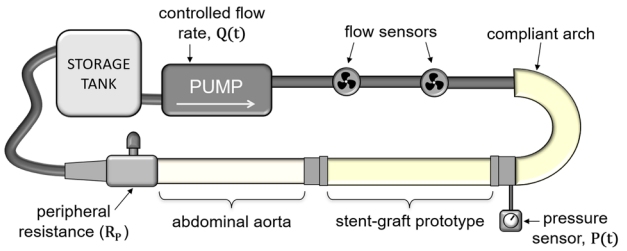



**Fig. 3 Diagram of the flow loop setup used for in vitro measurements of pressure change caused by the DWSG prototypes. The full model is designed to simulate the aorta and peripheral vasculature; the DWSG prototype is positioned in the descending thoracic aorta.**

onto a curved latex balloon base via a blotting technique (cf. [23]) to an approximate thickness of 3.8 mm. The arch was circumferentially reinforced at four locations with vinyl tape to restrict expansion and maintain relatively low compliance. The compliance of the arch was not experimentally quantified, but it remained constant throughout all experiments and was estimated through the Windkessel model optimization, as described later in Sec. 2.3.2. The prototype fixture enforced a DWSG length of 15 cm as in the static inflation tests, and it was mounted in the flow loop at a position representing the descending thoracic aorta. A 2.54 cm (1 in.) diameter semicompliant tube (Clearflex 60 PVC) downstream of the prototype fixture represented the abdominal aorta, followed by a needle valve that was set to emulate the peripheral vascular resistance and to maintain physiologic pressure ranges in the DWSG. The outlet of the needle valve was connected to the reservoir that fed the pump, thus forming a closed-loop. To maintain constant outlet pressure, the outlet drained above the fill level of the reservoir to open air. This required the outlet to be elevated above the inlet, but the resulting hydrostatic pressure was measured and subtracted off in all reports of pressure.

Flow rate was measured upstream of the arch with two flow-through meters (Gems Sensors, Plainville, CT) to capture the wide range of flow rates (0 to >100 mL/s) over each pump cycle. Pressure was measured at two locations in the system: directly upstream of the DWSG (Validyne) and upstream of the needle valve (Harvard Apparatus, Holliston, MA). Only measurements from the transducer upstream of the DWSG were used for the analyses in this paper.

Water was used as the working fluid in all experiments because viscous effects were not expected to have a major influence on the general behaviors observed for different DWSG prototypes. This expectation was reasonable based on the moderately high (~1000) average Reynolds number in the system, but some flow loop cases were duplicated with a high viscosity glycerol–water solution to verify that trends were consistent. The same trend in pulse pressure was found between the water and glycerol tests, but no discernable trend in peak pressure was found in the glycerol trials due to large variation in the mean pressure.

Both pressure transducers were zeroed at atmospheric pressure before connection to the flow loop, and lumen pressure was recorded with respect to the atmosphere. Measurements from the flow and pressure sensors were collected with a DAQ and MATLAB script as in the inflation experiments. Data collection was initiated for each trial after the pump had run at least 10 cycles at the current setting and was terminated after 30 s.

Pressure upstream of the DWSG was analyzed to extract a maximum, minimum, and mean value for each cycle. Data from all cycles were averaged and combined with other trials of the same test condition. Pulse pressure, defined as the difference between maximum and minimum pressures, was also calculated.

To evaluate the effect of the independent variables (gas charge, inner wall diameter, and inner wall prestretch) on pressure changes, normalized peak and pulse pressure data were both fit with linear models. The average pressure from each test condition was normalized against the zero-gas-charge pressure for the same inner wall configuration; this process set all of the zero-gas-charge cases to zero and removed the effect of mean pressure variability caused by perturbations to the reservoir level. The linear models (Eq. (2)) included noninteracting terms for gas charge $V_g$, ratio of inner wall to outer wall diameter $d$, and inner wall prestretch $\lambda$, with respective coefficients $c_V$, $c_d$, and $c_\lambda$. An additional coefficient $c_0$ specified the intercept for the equation.

$$\hat{P} = c_0 + c_V \cdot V_g + c_d \cdot d + c_\lambda \cdot \lambda \tag{2}$$

Equation (2) was used for both peak and pulse pressure models, so $\hat{P}$ is a placeholder variable that could refer to either normalized peak pressure or normalized pulse pressure. Coefficients for each pressure measure were found using the lm() function in RStudio [24]. Each data point was weighted by the inverse of its variance. The $P$ value for each coefficient being nonzero was found using a two-sided $t$-test, with the significance criterion set as $p < 0.05$.

*2.2.3 Experimental Design.* A total of 28 DWSG configurations were tested by varying inner wall diameter, inner wall prestretch, and gas charge (Table 1). These cases were compared to a rigid stent-graft case, in which zero gas charge was added to any of the DWSG prototypes. A smaller range of gas charges was tested when the inner wall prestretch was lower because the lumen became almost completely occluded at 60 mL gas charge, causing pressures to exceed measurable range. Flow loop experiments were conducted with the pump set to a stroke volume of 30 mL, with pulse rates of 40 and 60 beats per minute. Two additional runs with the same pulse rates and a stroke volume of 15 mL were conducted with zero gas charge to ensure that enough data were available for model optimization. The flow loop was modeled using a three-element Windkessel model, described below in Sec. 2.3.2.

**2.3 Computational Models.** Two different computational models were developed to describe the DWSG and predict its effect on blood pressure. In both models, performance of the DWSG is expressed in terms of resistance and capacitance.

*2.3.1 DWSG Finite Element Model.* An axisymmetric, quasi-static finite element (FE) model was developed to reproduce behavior observed in the static inflation experiments and to predict behavior for untested configurations. An axisymmetric model of the DWSG inner wall was created in ABAQUS (Dassault Systèmes, Vélizy-Villacoublay, France) using membrane-type elements to represent the thin latex tube. A mesh of the membrane with 200 elements was used for all computations. The outer wall was modeled as a fixed rigid boundary at a radius of 1.27 cm (½ in.). A prestretch condition was applied to the latex tube by holding one edge fixed and axially displacing the opposite edge by the appropriate distance. For tubes with a smaller radius than the outer wall, both edges were then displaced to a radius of 1.27 cm to simulate stretching the tube around the outer wall. The edges were held in this position for subsequent steps, in which a series of pressures was applied to the outer face of the tube, representing inflation of the DWSG with different gas charges. To

**Table 1 DWSG configurations tested in static and flow loop experiments**

| Inner wall diameter (cm) | Prestretch (%) | Gas charges (mL at $P = 1$ atm) |
|---|---|---|
| 1.91 (3/4 in.) | 5 | 10, 20, 30, 40, 50 |
| | 50 | 10, 20, 30, 40, 50, 60 |
| 2.22 (7/8 in.) | 5 | 10, 20, 30, 40, 50 |
| | 50 | 10, 20, 30, 40, 50, 60 |
| 2.54 (1 in.) | 50 | 10, 20, 30, 40, 50, 60 |

minimize computational cost, behavior of the confined gas was not considered in the FE model itself. Rather, the output of the model was the volume of the gas layer at different pressure differentials ($P_{gas} - P_{lumen}$) based only on mechanical stresses in the inner wall (Fig. 4(*a*)). Since only the transmembrane pressure difference matters in constructing the curve in Fig. 4(*a*), a family of $P_{gas} - P_{lumen}$ curves (solid lines in Fig. 4(*b*)) can be generated for different $P_{lumen}$ values simply by shifting the original curve. Additional information is available from the Ideal Gas Law ($P_1V_1 = P_2V_2$ for an isothermal, closed system), allowing the generation of a second set of $V_{gas}$ versus $P_{gas}$ curves (dashed lines in Fig. 4(*b*)). Thus, for a given $P_{lumen}$ and gas charge, the final configuration can be determined from the intersection of the two curves.

Next, a curve of $V_{lumen}$ versus $P_{lumen}$ was generated from the intersections in Fig. 4(*b*) at a series of $P_{lumen}$ values (Fig. 4(*c*)). The slope of this curve was calculated to specify the capacitance for that case. A different curve was generated for each gas charge, for each inner wall diameter, and for each prestretch level.

The flow resistance, $R$, of the DWSG was estimated for Poiseuille flow by integrating the inner wall radius, $r$, over the total axial length of the device, $L$,

$$R = \int_0^L \frac{8\mu}{\pi r^4} dx \tag{3}$$

where $r$ is a function of axial position $x$. The viscosity $\mu$ was set to $3.45 \times 10^{-3}$Pa · s for blood to calculate physiologically relevant resistance values, although water was used for the experiments.

*2.3.2 Windkessel Model.* The three-element Windkessel (Fig. 5(*a*)) [25] was first used to capture the behavior of the DWSG in the experimental flow loop system; then it was used with published parameter values for the arterial system to predict the effect of the DWSG on blood pressure in a patient.

*2.3.2.1 Flow loop model.* Because the flow loop system was built to mimic the human arterial system, it was reasonable to model it using the three-element Windkessel. We chose not to use the four-element Windkessel because it would provide only incremental improvement over the chosen model, and we wanted to minimize the number of parameters to estimate. One modification to the standard Windkessel was that the peripheral resistance $R_P$ had contribution from two sources,

$$R_P = R_{DWSG} + R'_P Q \tag{4}$$

where the linear component $R_{DWSG}$ accounted for the flow resistance introduced by the DWSG prototype, while $R'_P$ represented the needle valve, for which the pressure drop followed orifice flow behavior and had a squared relationship with flow rate $Q$. Note that the units of $R'_P$ must be different from a normal resistor, to

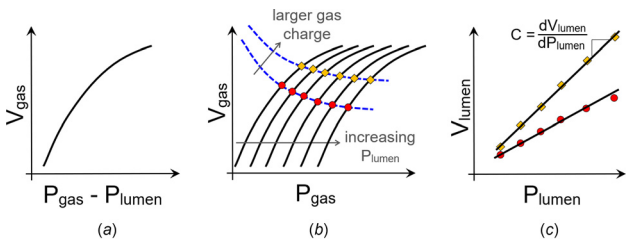



**Fig. 4 Workflow for calculating capacitance from the FE model, where (*a*) is an example curve due to inner wall deformation, and (*b*) shows that curve (solid lines) translated into gas volume versus pressure, with Ideal Gas Law curves (dashed) intersecting at points that give the true behavior of the DWSG system. In (*c*), those intersection points are plotted to show how the lumen volume changes with lumen pressure. The slope of this trend for a given gas charge is the DWSG capacitance.**

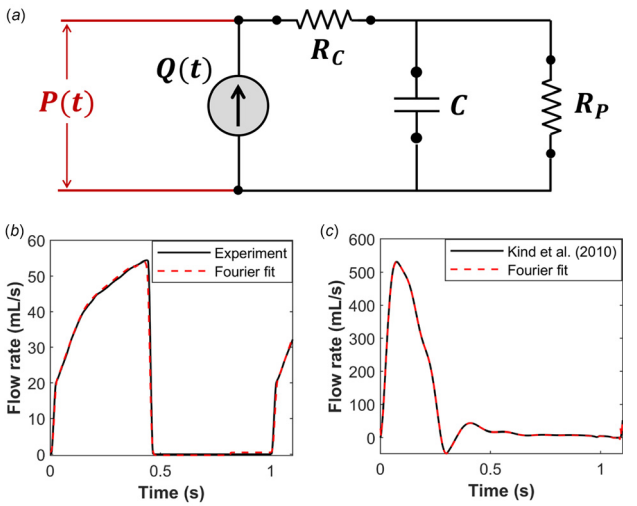



**Fig. 5 (*a*) Diagram of the three-element Windkessel model used to replicate flow loop measurements and predict physiologic behavior. *P*(*t*) is the pressure measurement across the system, *Q*(*t*) is the flow rate input, $R_C$ is the characteristic impedance, *C* is the capacitance, and $R_P$ is the peripheral resistance. (*b*) Input flow rate *Q*(*t*) used in the Windkessel model for the flow loop. Solid line is the measured flow from the flow experiments, and the dashed line is the Fourier series representation of that curve, which was used in Windkessel calculations. (*c*) Input flow rate *Q*(*t*) used in the Windkessel model of the human arterial system [27]. Solid line is the flow reported in the literature, and the dashed line is the Fourier series representation of that curve, which was used in Windkessel calculations.**

cancel the units of volumetric flow rate $Q$. The experimentally measured flow rate from the flow loop, $Q(t)$, was the input to the model (Fig. 5(*a*)), and the pressure drop across the system, $P(t)$, was the measured output. The model was evaluated in the frequency domain for the first 200 harmonics obtained when the flow rate was decomposed using a Fourier series (dashed curve, Fig. 5(*b*)) [26].

Parameter optimization was first conducted for a "rigid stent-graft" case, where the DWSG prototype had zero gas charge ($R_{DWSG} = 0$ in Eq. 4), so the inner wall was flush against the stiff outer wall. This case was used to find values for $R_C$, $C_0$, and $R'_P$, where $R_C$ was resistance of the system upstream of the DWSG prototype and $C_0$ represented capacitance of the elastic arch and other flexible tubing throughout the system. Parameters were determined using *fminsearch()* in MATLAB by minimizing the error between pressure waveforms in the model and in the experiment for a series of flow conditions. Half of the experiments were used to optimize the parameters, and the other half were used to assess the predictive capability of the model.

The optimization procedure was repeated for each nonzero gas charge, but now $R_C$, $C_0$, and $R'_P$ were held fixed and values for $C_{DWSG}$ and $R_{DWSG}$ were estimated. The value of $C_{DWSG}$, which represented capacitance of the DWSG prototype, was calculated by subtracting $C_0$ from the total capacitance output by the optimization. These estimates were compared to the capacitance and resistance values from static measurements in Secs. 2.2.1 and 2.3.1. We hypothesized that the static capacitance calculation would overpredict the apparent dynamic capacitance because the DWSG gas layer would not have time to fully compress over the course of a single pump stroke before expanding again when the flow rate (and pressure) dropped.

*2.3.2.2 Arterial model.* After we had completed the Windkessel parameter optimization for the flow loop experiment, the optimized DWSG parameters were used to make predictions about how the DWSG would affect blood pressure when implanted into

a human aorta. These predictions were made for both a normotensive and a hypertensive patient, to assess whether the DWSG would have different impact depending on the condition of the patient's arterial system. Characteristic impedance $R_C$ and peripheral resistance $R_P$ were set to values reported by Kind et al. [27] for normotensive and hypertensive patients.

In order to divide capacitance $C$ into the contributions of different aortic regions, a literature search was conducted to find average length $L_i$, radius $r_i$, wall thickness $h_i$, and stiffness $E_i$ for the ascending aorta and arch ($i = 1$), the descending aorta ($i = 2$), and the abdominal aorta ($i = 3$) [28–31]. The resistance $R_i$ of each segment was calculated using Eq. (3) and added to $R_P$. Resistance of the aorta is negligible compared to the peripheral resistance, but we included it in the total resistance in order to observe the effect of DWSG resistance at high gas charge. The capacitance $C_i$ of each aortic segment was calculated using Eq. (5), which was derived from Law of Laplace for thin-walled pressure vessels. Poisson's ratio $\nu = 0.5$ was used under the assumption that the vessel wall is incompressible. Table 2 summarizes the aortic properties and the calculated capacitance and resistance. The normotensive case was developed using the aortic properties reported for people under 30 years of age, and the hypertensive case used properties for people over 70 years

$$C_i = \frac{\left(1 - \frac{\nu}{2}\right)\pi r_i^3 L_i}{E_i h_i} \tag{5}$$

The capacitance values found via Eq. (5) were much larger than those typically reported for use in an arterial Windkessel model. To resolve this inconsistency, the values in Table 2 were used only to find the relative contribution of each aortic segment to the total capacitance. After establishing these proportions, the actual capacitance attributed to each segment was given by the total capacitance reported in Ref. [27] multiplied by the appropriate proportion.

Baseline blood pressures for the unstented cases were found by running the Windkessel model with literature values only [27]. Because the target location for the DWSG is the descending aorta, capacitance and resistance in this region were changed to simulate placement of different stent-graft configurations. Placement of a rigid stent-graft was modeled by setting $C_2 = 0\text{mL/mmHg}$ and leaving $R_2$ unchanged. For each DWSG case, the capacitance values were taken from the average Windkessel fits from Sec. 2.3.2.1. Resistance measurements were taken from the FE model

**Table 2 Properties of the aorta found in literature [28–31], used to calculate Windkessel parameters for aortic resistance *R* and capacitance *C***

| Regional property | | | | Age < 30 yr | Age > 70 yr |
|---|---|---|---|---|---|
| Ascending | $L_1$ | (cm) | [29] | $10.0 \pm 0.7$ | $13.1 \pm 1.4$ |
| | $r_1$ | (cm) | [29] | $1.38 \pm 0.14$ | $1.66 \pm 0.21$ |
| | $E_1$ | (kPa) | [30] | 13.5 | 100 |
| | $h_1$ | (cm) | [28] | 0.180 | 0.290 |
| | $C_1$ | (mL/mmHg) | | 3.40 | 0.649 |
| | $R_1$ | (mmHg·s/mL) | | $1.82 \times 10^{-4}$ | $1.14 \times 10^{-4}$ |
| Descending | $L_2$ | (cm) | [29] | $13.9 \pm 1.6$ | $14.3 \pm 1.3$ |
| | $r_2$ | (cm) | [29] | $1.03 \pm 0.08$ | $1.21 \pm 0.13$ |
| | $E_2$ | (kPa) | [30] | 13.9 | 56.8 |
| | $h_2$ | (cm) | [28] | 0.176 | 0.215 |
| | $C_2$ | (mL/mmHg) | | 1.95 | 0.652 |
| | $R_2$ | (mmHg·s/mL) | | $8.14 \times 10^{-4}$ | $4.40 \times 10^{-4}$ |
| Abdominal | $L_3$ | (cm) | [29] | 15 | 15 |
| | $r_3$ | (cm) | [29] | $0.91 \pm 0.07$ | $1.07 \pm 0.16$ |
| | $E_3$ | (kPa) | [31] | 51 | 337 |
| | $h_3$ | (cm) | [28] | 0.114 | 0.192 |
| | $C_3$ | (mL/mmHg) | | 0.611 | 0.0892 |
| | $R_3$ | (mmHg·s/mL) | | $1.44 \times 10^{-4}$ | $7.54 \times 10^{-4}$ |

(Sec. 2.3.1). A healthy aortic flow rate was used for $Q(t)$ with a pulse rate of 55 beats per minute (Fig. 5(*c*)) [27]. The systolic, diastolic, and mean pressures were calculated for each simulation and were compared to the unstented and rigid stent-graft pressures.

## 3 Results

Section 3.1 reviews the capacitance and resistance of the DWSG, as determined by the static model and experiments, as well as the Windkessel optimization. In Sec. 3.2, dynamic behavior of the DWSG is first evaluated within the experimental flow loop, and then predictions about physiologic pressure changes are made by using the capacitance and resistance values in the Windkessel model.

**3.1 Characterizing the Double-Walled Stent-Graft.** An example mesh from the FE model is shown in Fig. 6(*a*) for a series of gas charges, at two different lumen pressures. At a given lumen pressure, a higher gas charge led to smaller lumen volume. When lumen pressure was increased, the lumen volume also increased, for a given gas charge. For each inner wall configuration, there was a positive gas charge that led to zero pressure differential between the gas and the lumen. Adding more gas led to a positive gauge pressure in the gas layer, while adding less gas led to a negative gauge pressure. No notable discontinuities arose in DWSG behavior when transitioning between negative and positive gauge pressures.

*3.1.1 DWSG Capacitance.* Pressure–volume relationships for each DWSG case were obtained from both the FE model and the inflation experiment. The capacitance for each case was estimated by taking the slope of the pressure–volume relationship for lumen pressures between 40 and 250 mmHg. Linearity was a reasonable approximation within these bounds for both the model (Fig. 6(*b*)) and experiment (Fig. 6(*c*)), although both showed slightly

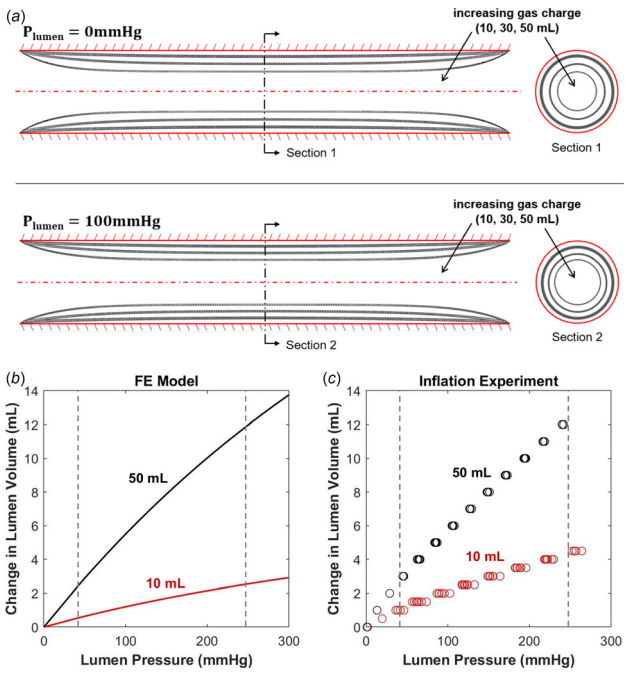



**Fig. 6 (*a*) Example FE model output for a range of gas charges at two lumenal pressures (0 and 100 mmHg). The pressure–volume relationships for two gas charges are shown for the FE model (*b*) and the inflation experiment (*c*). Dashed lines show bounds on lumen pressure, between which the slope was measured. All panels show results for the 1.91 cm (3/4 in.) diameter inner wall, 50% prestretch DWSG case.**

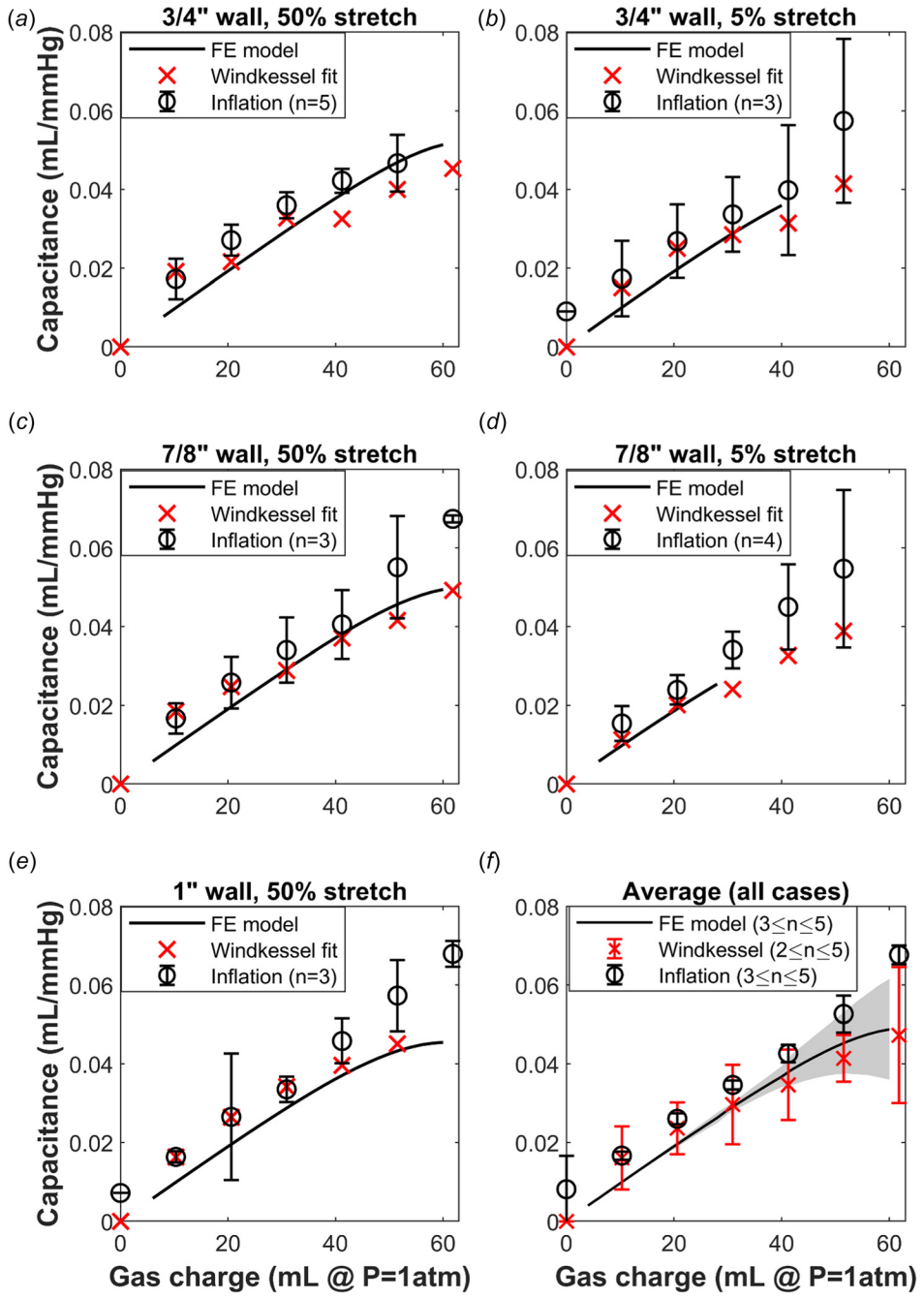



**Fig. 7 (*a*)–(*e*) Capacitance of different DWSG cases, as measured by the FE model, the Windkessel model fit to flow experiments, and the inflation experiments. Rows separate inner wall diameters and columns separate inner wall prestretches. (*f*) Average capacitance over all cases for both models and the experiment. All error bars show 95% CIs.**

sublinear behavior. Given that the FE model parameters were not adjusted to fit the experiments, the agreement between the model predictions (Fig. 6(*b*)) and the experimental measurements (Fig. 6(*c*)) was quite good. The model could not be evaluated for all cases because buckling of the inner wall caused the model to fail; this behavior was observed most often with high gas charges.

Another estimate of capacitance was obtained by fitting the flow loop experiments to a Windkessel model. Parameters of the system were obtained through an optimization routine that minimized error between Windkessel-predicted and experimentally measured pressure profiles when the rigid stent-graft was placed. DWSG resistance and capacitance were found by repeating the optimization for each case and subtracting off the values from the rigid case. This procedure assumed that both resistance and capacitance of the rigid stent-graft prototype were negligible, which was consistent with zero-gas measurements obtained with the other methods.

Figure 7 compares capacitance measurements from the static FE model, the inflation experiments, and the Windkessel fit for each DWSG case. An increase in capacitance was observed with larger gas charge for all inner wall diameters at both prestretch levels. The three measurement techniques were in good agreement with each other. For all five cases (Fig. 7(*a*)–7(*e*)), the FE model underpredicted the experimentally measured capacitance, possibly due to nonzero compliance of the outer wall in the prototypes used with the experiment. This discrepancy is clear when looking

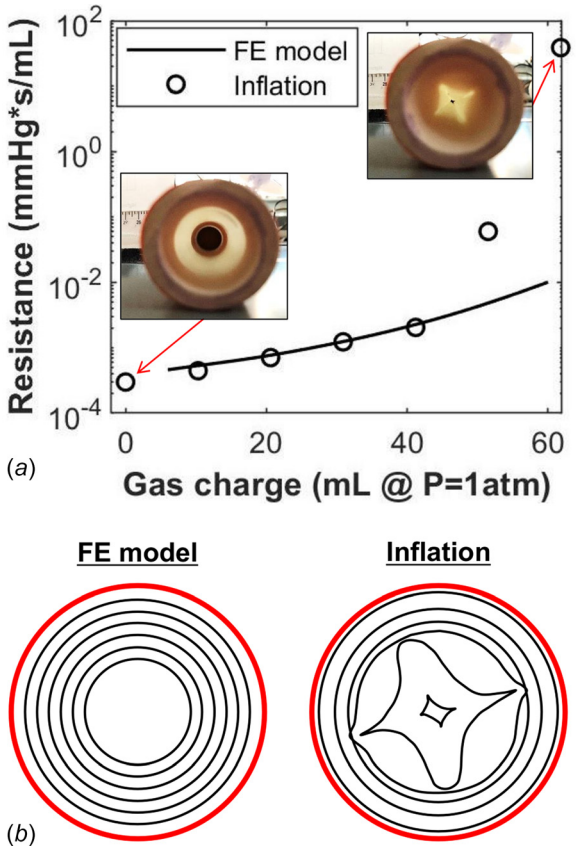



**Fig. 8 (*a*) Poiseuille resistance of the 1.91 cm (¾ in.) diameter, 50% prestretch inner wall DWSG case, calculated from the FE model and the prototype inflation. Photos of the prototype show the lumen cross section for 0 and 60 mL gas charges. (*b*) Comparison of cross-sectional profiles for the model and prototype from 10 to 60 mL gas charge (outside to inside). Each ring shows the position of the inner wall at a given gas charge, when a cross section is taken at the midpoint along the axial length. The thick outer ring represents zero gas charge, when the inner wall is flat against the outer wall.**

at the average capacitance over all inner wall configurations for each gas charge (Fig. 7(*f*)), where the FE model trends toward zero capacitance at zero gas charge, whereas a capacitance of $0.0081 \pm 0.0085$ mL/mmHg was measured for zero gas charge in the experiment. The method for calculating capacitance with the Windkessel model also led to zero capacitance at zero gas charge, so these values tend to align more with the FE model than the inflation experiment.

For any given gas charge, there was very little difference in capacitance among the different inner wall configurations. The FE model showed some dependence on inner wall configuration at large gas charges, as seen by a wider confidence interval in the calculated average capacitance (Fig. 7(*f*)); this dependence was not evident from the inflation or Windkessel methods. Overall, a linear relationship between gas charge and capacitance was apparent, especially at lower gas charges.

*3.1.2 DWSG Resistance.* The flow resistance of each DWSG configuration was calculated using Eq. (2), with radius measurements from the FE model and the prototypes. In cases where the inner wall of the prototype had buckled, the hydraulic diameter at the narrowest cross section was used in the equation. Figure 8(*a*) shows resistance measurements for the 1.91 cm (¾ in.) diameter, 50% prestretch inner wall case. There is good agreement between the model and prototype until the inner wall of the prototype has buckled at 50 mL gas charge, causing the resistance to spike. Figure 8(*b*) shows the profile of the DWSG inner wall for gas charges from 10 to 60 mL for the FE model and the inflation. The FE model did not predict that the inner wall would buckle until above 60 mL gas charge, but the premature buckling in the inflation could be explained by a natural crease present in the latex tubing that was used to construct the inner wall of the prototype. The crease is visible in Fig. 8(*b*) at 40 mL gas charge before full buckling has occurred at 50 mL charge.

Resistance from the Windkessel fit was not comparable to the static measurements because the low viscosity of water (used in the flow experiments) caused the values to be extremely small ($\sim 10^{-12}$ mmHg·s/mL). Minor variability in the mean pressure in the flow loop, due to changing reservoir level between experiments, caused significant variation in the fitted resistance.

### 3.2 Dynamic Behavior

*3.2.1 Flow Loop Measurements.* The effect of different DWSG configurations on dynamic pressure was measured in an in vitro flow loop. Although multiple flow rates were tested to conduct Windkessel optimization, only the 60 beats/min, 30 mL stroke volume flow case was used when reporting pressure changes. Figure 9(*a*) shows an example pressure profile from the flow loop measurements (solid line) and the corresponding fit achieved with the Windkessel model (dashed line).

As gas charge was increased, peak pressure (Fig. 9(*b*)) and pulse pressure (Fig. 9(*c*)) both decreased. At 60 mL gas charge, an 8% reduction in peak pressure was observed with respect to the rigid stent-graft case (Fig. 9(*d*)). Pulse pressure changed more significantly, with a 24% decrease compared to the rigid case (Fig. 9(*e*)). Different inner wall configurations for the DWSG appeared to have negligible effect on system pressure. This observation is consistent with the static results that showed the gas charge dominating the capacitance and resistance measurements.

The normalized peak and pulse pressure data (Fig. 9(*d*) and 9(*e*)) were both fit to linear models of the form given in Eq. 2. The coefficients and their corresponding $P$ values are reported in Table 3. For both the peak and pulse pressure measures, the only variable with significant contribution to the pressure change was gas charge. Normalized peak pressure exhibited a negative dependence on gas charge with $c_V = -0.134 \pm 0.005$ mL$^{-1}$ (mean ± SE), while normalized pulse pressure showed a stronger correlation with $c_V = -0.372 \pm 0.013$ mL$^{-1}$. The P value for both of these coefficients was well below the cutoff for significance. The coefficient for inner wall diameter $c_d$ was significant in the pulse pressure model ($p = 0.048$), though the uncertainty in the coefficient value was quite large ($c_d = -6.67 \pm 3.22$).

*3.2.2 Physiologic Predictions With the Windkessel Model.* The Windkessel model was evaluated to predict the effect of the DWSG versus a rigid stent-graft when placed in the descending thoracic aorta of normotensive and hypertensive patient models. DWSG capacitance and resistance were defined using values from the FE model (Table 4). Because inner wall properties were not found to be significant, the average values for each gas charge were used in this model. Flow rate $Q(t)$ was set to a physiologic signal, and the resulting pressure profiles from the rigid stent-graft case are shown in Fig. 10(*a*). The hypertensive case had significantly higher pressures compared to the normotensive case for all gas charges.

Increasing gas charge always decreased both the peak and pulse pressure (Figs. 10(*b*) and 10(*c*)), but neither measure returned to the unstented value for even the largest gas charge (60 mL). Figure 10(*d*) shows that a rigid stent-graft increased peak pressure by 25% in a hypertensive patient and 10% in a normotensive patient, compared to the pressure in the unstented aorta. At maximum gas charge, this pressure increase compared to the unstented case was only 19% in the hypertensive patient, while the 10% increase persisted for the normotensive patient. The rigid stent-graft had a greater effect on pulse pressure (Fig. 10(*e*)) with 72% and 40% increases for the hypertensive and normotensive patients,

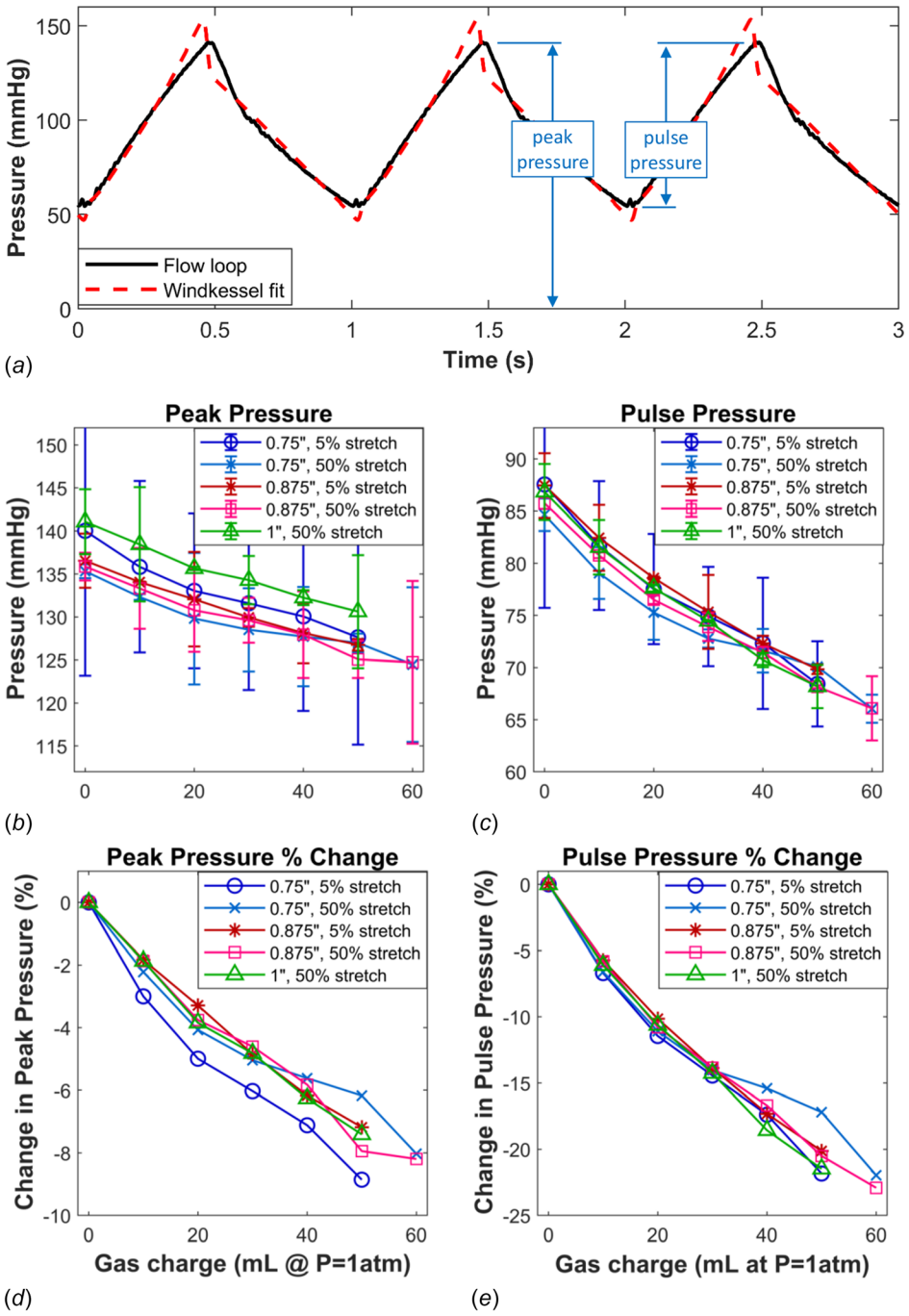



**Fig. 9 (*a*) Example pressure wave measured from the flow loop (solid line), with the Windkessel fit for that measurement shown with a dashed line. The definitions for peak and pulse pressures are identified with arrows on the plot. (*b*) Peak pressure and (*c*) pulse pressure for each DWSG case as a function of gas charge; 95% CI shown for $n = 2$. (*d*) Percent change in peak pressure and (*e*) pulse pressure; CI omitted from (*d*) and (*e*) for clarity.**

respectively. The increase in pulse pressure reduced to 66% at 60 mL gas charge for the hypertensive patient, while it decreased to 35% for the normotensive patient. In Fig. 10(*d*), it appears that the normotensive patient would receive maximum benefit at 50 mL gas charge, with pressure increasing slightly for 60 mL. This result reminds us that a balance must be maintained between the benefit of increased capacitance and the cost of increased fluid resistance.

## 4 Discussion

**4.1 Double-Walled Stent-Graft Design.** We have created a double-walled aortic stent-graft design with the goal of addressing the issue of persistent high blood pressure in patients who receive standard, inextensible stent-grafts. The design leverages the compressibility of biocompatible gas to provide fluid capacitance to the arterial system without requiring the aorta itself to be distensible. Prototypes of the design were fabricated with PVC tubing for the stiff outer wall and latex tubing for the flexible inner wall. Different gas charges and inner wall diameters were compared. The impact of inner wall stiffness was also evaluated by prestretching the inner walls to different levels before mounting them in the prototype. These simplified prototype models were used to assess the pressure-reduction capability of the design and to identify which parameters had the greatest effect on this capability.

**Table 3 Coefficients for the linear models relating normalized peak and pulse pressures to gas charge ($c_V$), inner wall diameter ($c_d$), and inner wall stretch ($c_\lambda$)**

| | Coefficients | Value ± SE | *P* value |
|---|---|---|---|
| Peak pressure | $c_0$ | $-0.322 \pm 1.322$ | 0.809 |
| | $c_V$ (1/mL) | $-0.134 \pm 0.005$ | $<2 \times 10^{-16}$ |
| | $c_d$ | $-1.115 \pm 1.183$ | 0.354 |
| | $c_\lambda$ | $0.527 \pm 0.559$ | 0.354 |
| Pulse pressure | $c_0$ | $2.429 \pm 3.448$ | 0.487 |
| | $c_V$ (1/mL) | $-0.372 \pm 0.013$ | $<2 \times 10^{-16}$ |
| | $c_d$ | $-6.670 \pm 3.219$ | 0.048 |
| | $c_\lambda$ | $1.038 \pm 1.521$ | 0.500 |

Model intercept is given by $c_0$. SE refers to the standard error. *P* values reported from a two-sided *t* test.

**Table 4 Capacitance and resistance measurements of the DWSG used for physiologic predictions in the Windkessel model. Reported as mean ± 95% CI.**

| Gas charge (mL) | Capacitance (mL/mmHg) | Resistance ($\times 10^{-4}$ mmHg·s/mL) |
|---|---|---|
| 0 | 0 | 3.85 |
| 10 | $0.0160 \pm 0.0081$ | $5.19 \pm 0.14$ |
| 20 | $0.0236 \pm 0.0066$ | $7.34 \pm 0.36$ |
| 30 | $0.0296 \pm 0.0101$ | $11.0 \pm 1.4$ |
| 40 | $0.0346 \pm 0.0089$ | $19.0 \pm 5.3$ |
| 50 | $0.0414 \pm 0.0060$ | $39 \pm 16$ |
| 60 | $0.0472 \pm 0.0172$ | $86 \pm 68$ |

This preliminary study served as a means to demonstrate that a small volume of gas could cause meaningful pressure reduction in a system with conditions comparable to in vivo. The DWSG prototypes were built to allow the amount of gas and the inner wall properties to be changed easily, while the outer wall remained unchanged as an essentially rigid boundary. Although standard stent-grafts are not completely rigid, we used a rigid outer wall to isolate and quantify the effect of the gas compression in the DWSG prototypes. Any additional benefit from a more compliant outer wall would depend on compliance of the native aorta within which the device is placed.

Results from this preliminary study have encouraged us to proceed with designing a more realistic DWSG prototype that can be tested within ex vivo cadaveric models and in animal models. Moving forward with development of the DWSG, we will need to address a handful of design challenges. The material selected for the inner wall must be highly impermeable to $CO_2$, to prevent reduced performance of the DWSG due to gradual diffusion of the gas layer. The results of our preliminary work have shown that the mechanical properties of the inner wall have little effect on the behavior of the DWSG, as long as the wall is flexible enough to transmit lumenal pressure to the gas. This finding means that the wall material can be optimized to minimize gas exchange. To further address the potential for gas leakage, the final design will incorporate several independent gas pockets, such that the gas layer resembles bubble wrap or closed-cell foam. Though this compartmentalization will reduce the amount of gas that can be contained for a given reduction in lumenal area, it will ensure that puncture or leakage from one region will not disable the entire system. Dynamic flow simulations will be conducted to find a configuration of gas pockets that causes the least flow disturbance.

Another uncertainty is how the DWSG will be deployed percutaneously through a catheter of similar diameter to those used with current stent-graft systems. To crimp the DWSG to a small enough size, the gas will need to be added after deployment in the aorta. Strategies for remote inflation will be drawn from existing products such as the Nellix EndoVascular Aneurysm Sealing System [32] and other devices that are filled with fluid percutaneously and then disconnected from the filling system.

**4.2 Double-Walled Stent-Graft Capacitance and Resistance.** The only design parameter in this study that was found to affect the DWSG capacitance significantly was the amount of gas loaded into the space between the inner and outer walls. As expected, a larger gas charge led to larger capacitance values but also higher flow resistance. The DWSG resistance remained several orders of magnitude below the resistance of the peripheral vasculature up to a charge of about 60 mL, at which point the inner wall of some of the prototypes had completely collapsed and would not allow sufficient flow to pass through. This behavior was more severe in cases where the inner wall was stretched to only 5%, indicating that stiffness of the inner wall material will be an important parameter to investigate further. The FE model, which successfully captured the behavior of the DWSG prototypes at gas charges up to 40 mL, will be an important tool that can be used to further investigate the design space as it relates to capacitance and resistance measurements.

**4.3 Pressure Reduction With the Double-Walled Stent-Graft Design.** Flow loop testing and the Windkessel model both showed that the DWSG led to reduced pressure compared to a rigid stent-graft. Inner wall diameter and prestretch did not significantly affect this behavior, whereas both peak and pulse pressure decreased linearly with increased gas charge. This behavior was apparent in Figures 9(*b*)–9(*e*) and was confirmed by analyzing the coefficients of a linear model. The increase in flow resistance caused by the narrowed lumen of the DWSG did not appear to affect pressure even at high gas charge in the flow loop, suggesting that the benefit of increased capacitance outweighs the adverse effect of decreased flow area. Although the flow loop was designed to mimic the arterial system, some limitations of this system were a simplified inflow waveform, nonlinear peripheral resistance, and use of water as a working fluid. Although these were limitations in the physical flow loop model, they did not apply to simulations done with the Windkessel model. One concern with using water for the dynamic experiments was that flow resistance from the narrowed DWSG lumen would be underpredicted in comparison to the physiologic case where higher viscosity blood would flow through the same area. In the Windkessel model, with the fluid given blood viscosity, we still observed a trend of decreasing peak and pulse pressures as gas charge increased. The magnitude of pressure reduction in the Windkessel model was attenuated compared to the experimental results; this attenuation could be explained if the pressure decrease from DWSG capacitance was being more strongly counteracted by the pressure increase due to DWSG resistance.

The physiologic Windkessel model, with DWSG parameters set from the flow loop experiments, predicted a less substantial pressure reduction than was seen in the flow loop. This diminished effect could be explained by the higher fluid viscosity in this model, as described above, or by the significant compliance that the native arterial system has outside of the stented region. Consistent with that explanation, a simulated hypertensive patient saw greater benefit from the DWSG because the descending aorta contributed more to the overall capacitance and constituted a greater loss when made rigid via stenting. In both the hypertensive and normotensive simulated patients, a 15 cm DWSG was not able to restore pressure to unstented values, but this was in a model with a compliant proximal aortic arch and a stented descending aortic segment. We suspect that for a patient with pathology resulting in significantly diminished native aortic compliance, approaching the characteristics of the rigid outer graft, the DWSG may show actual improvement in hemodynamics. It is worth noting that even a 10 mmHg reduction in systolic pressure has been shown to decrease the risk of cardiovascular disease by 20% [33].

There is preliminary evidence that the DWSG could improve cardiovascular outcomes over standard stent-grafts, but our next

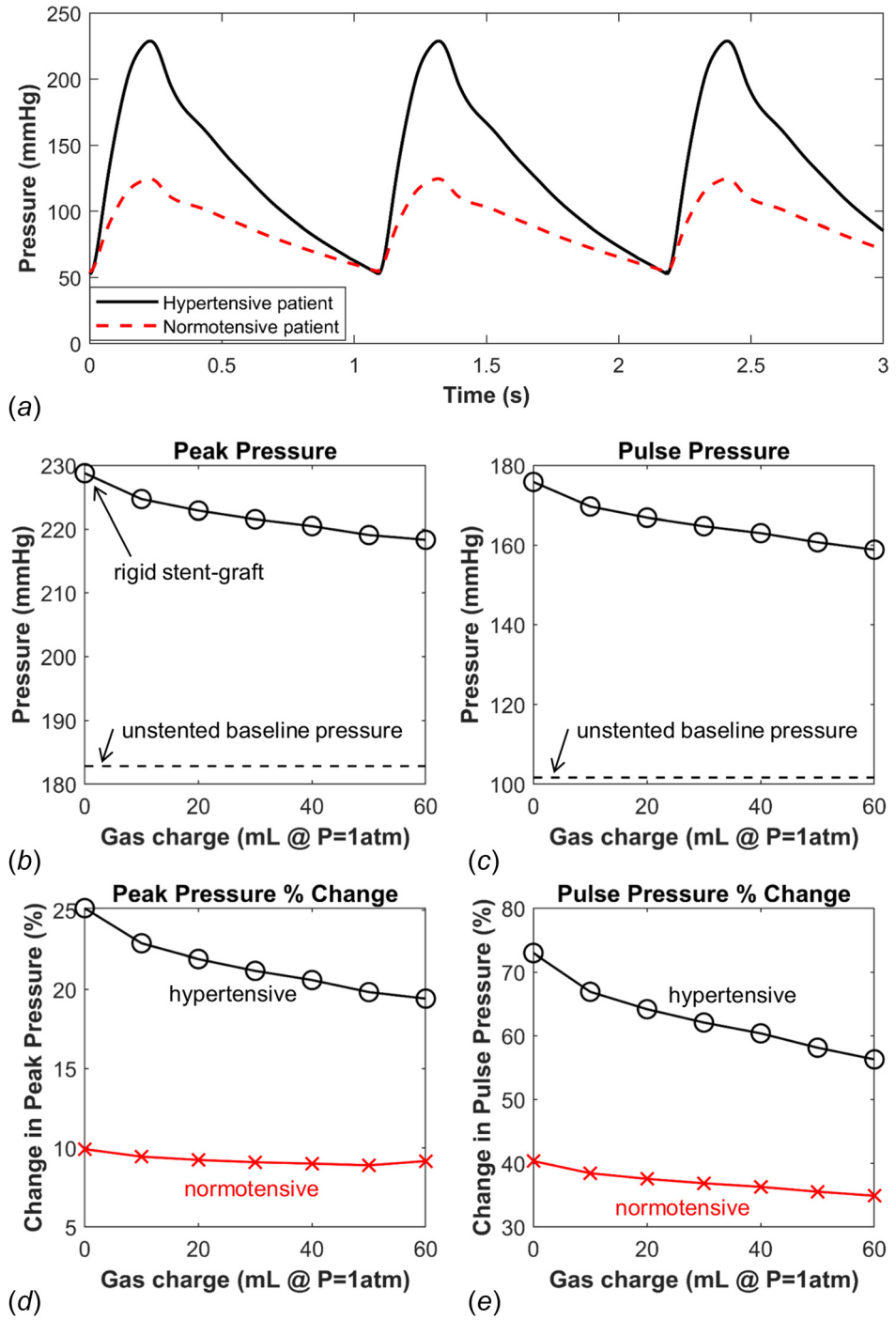



**Fig. 10** (*a*) **Example pressure waves for hypertensive (solid line) and normotensive (dashed line) patients with a rigid stent-graft, as predicted by the Windkessel model with physiologic input parameters [27]. (*b*) Peak pressure and (*c*) pulse pressure for each DWSG gas charge, as predicted by the physiologic Windkessel model. The baseline pressure with no stent-graft is shown by the dashed line in both (*b*) and (*c*). Only the hypertensive case is shown for clarity, due to a large difference in pressure range compared to the normotensive case. Percent change in (*d*) peak pressure and (*e*) pulse pressure, compared to the unstented condition for both hypertensive ("o") and normotensive ("x") cases.**

step is to gain a deeper understanding of the hemodynamic effect that the DWSG has in patients with a range of aortic properties. We saw that the narrowed lumen of the DWSG introduced negligible flow resistance into the system, but local flow behavior (turbulence, stagnation zones, wall shear stress) at the DWSG-aorta interface could not be characterized through the methods in this study. Development of a fluid–structure interaction model will give us the opportunity to evaluate different DWSG configurations in models with various physiologic flow conditions, vessel stiffnesses, and aortic geometries. A challenge with the fluid–structure interaction model is that the gas layer, contained by the flexible inner wall, introduces both another fluid phase and the need for membrane physics in the simulation. We are currently working to create a solid analog to capture the DWSG behavior to

make the simulations less complex. With information from the present study and future hemodynamic analyses, we will be able to identify the patient parameters (including stent-graft location, vessel compliance, peripheral vascular resistance, etc.) that are best suited to benefit from the DWSG design.

## Acknowledgment

The Anatomy Bequest Program at the University of Minnesota generously provided equipment used for the flow loop experiments in this work. The content is solely the responsibility of the authors and does not necessarily represent the official views of the National Institutes of Health's National Center for Advancing Translational Sciences.

## Funding Data

- National Institutes of Health's National Center for Advancing Translational Sciences (NIH NCATS) (Grant Nos. TL1R002493 and UL1TR002494; Funder ID: 10.13039/100006108).
- Funding was also provided by National Institutes of Health's National Heart, Lung, and Blood Institute (NIH NHLBI) (Grant No. U01HL139471; Funder ID: 10.13039/100000050).

## Nomenclature

$c$ = linear model coefficient
$C$ = fluid capacitance
$d$ = ratio of inner wall diameter (unstretched) to outer wall diameter
DWSG = double-walled stent-graft
$E$ = tangent modulus
FE = finite element
$h$ = wall thickness
$L$ = length
$P$ = pressure
$Q$ = volumetric flow rate
$r$ = lumen radius
$R$ = flow resistance
$V$ = volume
$V_g$ = gas charge (volume at atmospheric pressure)
$\lambda$ = inner wall prestretch
$\mu$ = dynamic viscosity
$\nu$ = Poisson's ratio

## References

[1] Benjamin, E. J., Blaha, M. J., Chiuve, S. E., Cushman, M., Das, S. R., Deo, R., de Ferranti, S. D., Floyd, J., Fornage, M., Gillespie, C., Isasi, C. R., Jiménez, M. C., Jordan, L. C., Judd, S. E., Lackland, D., Lichtman, J. H., Lisabeth, L., Liu, S., Longenecker, C. T., Mackey, R. H., Matsushita, K., Mozaffarian, D., Mussolino, M. E., Nasir, K., Neumar, R. W., Palaniappan, L., Pandey, D. K., Thiagarajan, R. R., Reeves, M. J., Ritchey, M., Rodriguez, C. J., Roth, G. A., Rosamond, W. D., Sasson, C., Towfighi, A., Tsao, C. W., Turner, M. B., Virani, S. S., Voeks, J. H., Willey, J. Z., Wilkins, J. T., Wu, J. H., Alger, H. M., Wong, S. S., and Muntner, P., 2017, "Heart Disease and Stroke Statistics—2017 Update a Report From the American Heart Association," Circulation, **135**(10), pp. e146–e603.
[2] Lewington, S., Clarke, R., Qizilbash, N., Peto, R., and Collins, R., 2002, "Age-Specific Relevance of Usual Blood Pressure to Vascular Mortality: A Meta-Analysis of Individual Data for One Million Adults in 61 Prospective Studies," Lancet, **360**(9349), pp. 1903–1913.
[3] Vasan, R. S., Larson, M. G., Leip, E. P., Evans, J. C., O'Donnell, C. J., Kannel, W. B., and Levy, D., 2001, "Impact of High-Normal Blood Pressure on the Risk of Cardiovascular Disease," N. Engl. J. Med., **345**(18), pp. 1291–1297.
[4] Stamler, J., Stamler, R., and Neaton, J. D., 1993, "Blood Pressure, Systolic and Diastolic, and Cardiovascular Risks: U.S. Population Data," Arch. Intern. Med., **153**(5), pp. 598–615.
[5] Swerdlow, N. J., Wu, W. W., and Schermerhorn, M. L., 2019, "Open and Endovascular Management of Aortic Aneurysms," Circ. Res., **124**(4), pp. 647–661.
[6] Harky, A., Chan, J. S. K., Wong, C. H. M., and Bashir, M., 2019, "Open Versus Endovascular Repair of Descending Thoracic Aortic Aneurysm Disease: A Systematic Review and Meta-Analysis," Ann. Vasc. Surg., **54**, pp. 304–315.
[7] Szeto, W. Y., McGarvey, M., Pochettino, A., Moser, G. W., Hoboken, A., Cornelius, K., Woo, E. Y., Carpenter, J. P., Fairman, R. M., and Bavaria, J. E., 2008, "Results of a New Surgical Paradigm: Endovascular Repair for Acute Complicated Type B Aortic Dissection," Ann. Thorac. Surg., **86**(1), pp. 87–94.
[8] Hansen, T. W., Staessen, J. A., Torp-Pedersen, C., Rasmussen, S., Thijs, L., Ibsen, H., and Jeppesen, J., 2006, "Prognostic Value of Aortic Pulse Wave Velocity as Index of Arterial Stiffness in the General Population," Circulation, **113**(5), pp. 664–670.
[9] Mitchell, G. F., 2014, "Recent Advances in Hypertension: Arterial Stiffness and Hypertension," Hypertension, **64**(1), pp. 13–18.
[10] Tremblay, D., Zigras, T., Cartier, R., Leduc, L., Butany, J., Mongrain, R., and Leask, R. L., 2009, "A Comparison of Mechanical Properties of Materials Used in Aortic Arch Reconstruction," Ann. Thorac. Surg., **88**(5), pp. 1484–1491.
[11] Dong, Z. H., Fu, W. G., Wang, Y. Q., Guo, D. Q., Xu, X., Ji, Y., Chen, B., Jiang, J. H., Yang, J., Shi, Z. Y., Zhu, T., and Shi, Y., 2009, "Retrograde Type a Aortic Dissection After Endovascular Stent Graft Placement for Treatment of Type B Dissection," Circulation, **119**(5), pp. 735–741.
[12] Azadani, A. N., Chitsaz, S., Mannion, A., Mookhoek, A., Wisneski, A., Guccione, J. M., Hope, M. D., Ge, L., and Tseng, E. E., 2013, "Biomechanical Properties of Human Ascending Thoracic Aortic Aneurysms," Ann. Thorac. Surg., **96**(1), pp. 50–58.
[13] Safar, M. E., O'Rourke, M. F., and Frohlichilkj, E. D., eds., 2014, *Blood Pressure and Arterial Wall Mechanics in Cardiovascular Diseases*, Springer-Verlag, Berlin.
[14] Sachs, T., Pomposelli, F., Hagberg, R., Hamdan, A., Wyers, M., Giles, K., and Schermerhorn, M., 2010, "Open and Endovascular Repair of Type B Aortic Dissection in the Nationwide Inpatient Sample," J. Vasc. Surg., **52**(4), pp. 860–866.
[15] Aquaro, G. D., Cagnolo, A., Tiwari, K. K., Todiere, G., Bevilacqua, S., Di Bella, G., Ait-Ali, L., Festa, P., Glauber, M., and Lombardi, M., 2013, "Age-Dependent Changes in Elastic Properties of Thoracic Aorta Evaluated by Magnetic Resonance in Normal Subjects," Interact. Cardiovasc. Thorac. Surg., **17**(4), pp. 674–679.
[16] Moulakakis, K. G., Kadoglou, N. P. E., Antonopoulos, C. N., Mylonas, S. N., Kakisis, J., Papadakis, I., Karakitsos, P., and Liapis, C. D., 2017, "Changes in Arterial Stiffness and N-Terminal pro-Brain Natriuretic Peptide Levels After Endovascular Repair of Descending Thoracic Aorta," Ann. Vasc. Surg., **38**, pp. 220–226.
[17] Vorp, D. A., Mandarino, W. A., Webster, M. W., and Gorcsan, J., 1996, "Potential Influence of Intraluminal Thrombus on Abdominal Aortic Aneurysm as Assessed by a New Non-Invasive Method," Cardiovasc. Surg., **4**(6), pp. 732–739.
[18] Schurink, G. W. H., Aarts, N. J. M., Wilde, J., Van Baalen, J. M., Chuter, T. A. M., Kool, L. J. S., and Van Bockel, J. H., 1998, "Endoleakage After Stent-Graft Treatment of Abdominal Aneurysm: Implications on Pressure and Imaging - An In Vitro Study," J. Vasc. Surg., **28**(2), pp. 234–241.
[19] Faizer, R., Barocas, V., Coletti, F., Kizilski, S., Datta, A., and Amili, O., 2018, "Compliant Aortic Stent Grafts and Related Systems and Methods," Patent No. 20200188084.
[20] Zamir, M., 2005, *The Physics of Coronary Blood Flow*, Springer Science+Business Media, Inc., Berlin.
[21] Cho, K. J., 2015, "Carbon Dioxide Angiography: Scientific Principles and Practice," Vasc. Spec. Int., **31**(3), pp. 67–80.
[22] Schindelin, J., Arganda-Carreras, I., Frise, E., Kaynig, V., Longair, M., Pietzsch, T., Preibisch, S., Rueden, C., Saalfeld, S., Schmid, B., Tinevez, J. Y., White, D. J., Hartenstein, V., Eliceiri, K., Tomancak, P., and Cardona, A., 2012, "Fiji: An Open-Source Platform for Biological-Image Analysis," Nat. Methods, **9**(7), pp. 676–682.
[23] Matthys, K. S., Alastruey, J., Peiró, J., Khir, A. W., Segers, P., Verdonck, P. R., Parker, K. H., and Sherwin, S. J., 2007, "Pulse Wave Propagation in a Model Human Arterial Network: Assessment of 1-D Numerical Simulations Against In Vitro Measurements," J. Biomech., **40**(15), pp. 3476–3486.
[24] RStudio Team, 2019, "RStudio: Integrated Development Environment for R," RStudio, PBC, Boston, MA.
[25] Westerhof, N., Lankhaar, J. W., and Westerhof, B. E., 2009, "The Arterial Windkessel," Med. Biol. Eng. Comput., **47**(2), pp. 131–141.
[26] Segers, P., Rietzschel, E. R., De Buyzere, M. L., Stergiopulos, N., Westerhof, N., Van Bortel, L. M., Gillebert, T., and Verdonck, P. R., 2008, "Three-and-Four-Element Windkessel Models: Assessment of Their Fitting Performance in a Large Cohort of Healthy Middle-Aged Individuals," Proc. Inst. Mech. Eng. Part H: J. Eng. Med., **222**(4), pp. 417–428.
[27] Kind, T., Faes, T. J. C., Lankhaar, J. W., Vonk-Noordegraaf, A., and Verhaegen, M., 2010, "Estimation of Three- and Four-Element Windkessel Parameters Using Subspace Model Identification," IEEE Trans. Biomed. Eng., **57**(7), pp. 1531–1538.
[28] Cuomo, F., Roccabianca, S., Dillon-Murphy, D., Xiao, N., Humphrey, J. D., and Figueroa, C. A., 2017, "Effects of Age-Associated Regional Changes in Aortic Stiffness on Human Hemodynamics Revealed by Computational Modeling," PLoS One, **12**(3), p. e0173177.
[29] Redheuil, A., Yu, W. C., Mousseaux, E., Harouni, A. A., Kachenoura, N., Wu, C. O., Bluemke, D., and Lima, J. A. C., 2011, "Age-Related Changes in Aortic Arch Geometry: Relationship With Proximal Aortic Function and Left Ventricular Mass and Remodeling," J. Am. Coll. Cardiol., **58**(12), pp. 1262–1270.
[30] Redheuil, A., Yu, W. C., Wu, C. O., Mousseaux, E., De Cesare, A., Yan, R., Kachenoura, N., Bluemke, D., and Lima, J. A. C., 2010, "Reduced Ascending Aortic Strain and Distensibility: Earliest Manifestations of Vascular Aging in Humans," Hypertension, **55**(2), pp. 319–326.
[31] Länne, T., Sonesson, B., Bergqvist, D., Bengtsson, H., and Gustafsson, D., 1992, "Diameter and Compliance in the Male Human Abdominal Aorta: Influence of Age and Aortic Aneurysm," Eur. J. Vasc. Surg., **6**(2), pp. 178–184.
[32] Batagini, N. C., Hardy, D., Clair, D. G., and Kirksey, L., 2016, "Nellix Endovascular Aneurysm Sealing System: Device Description, Technique of Implantation, and Literature Review," Semin. Vasc. Surg., **29**(1–2), pp. 55–60.
[33] Ettehad, D., Emdin, C. A., Kiran, A., Anderson, S. G., Callender, T., Emberson, J., Chalmers, J., Rodgers, A., and Rahimi, K., 2016, "Blood Pressure Lowering for Prevention of Cardiovascular Disease and Death: A Systematic Review and Meta-Analysis," Lancet, **387**(10022), pp. 957–967.